The Astrophysical Journal, 986:210 (11pp), 2025 June 20 https://doi.org/10.3847/1538-4357/add532

X-Ray Polarization in SN 1006 Southwest Shows Spatial Variations and Differences in the Radio Band

Ping Zhou[1,2], Patrick Slane[3], Dmitry Prokhorov[4], Jacco Vink[5], Riccardo Ferrazzoli[6], William Cotton[7,8], Niccolò Bucciantini[9,10,11], Yi-Jung Yang[12,13], Stefano Silvestri[14], Douglas A. Swartz[15], Philip Kaaret[16], Enrico Costa[6], C.-Y. Ng[17], Estela Reynoso[18], Paolo Soffitta[6], Allyn F. Tennant[16], Wenlang He[1], and David Moffett[19]

[1] School of Astronomy & Space Science, Nanjing University, 163 Xianlin Avenue, Nanjing 210023, People's Republic of China; pingzhou@nju.edu.cn
[2] Key Laboratory of Modern Astronomy and Astrophysics, Nanjing University, Ministry of Education, Nanjing 210023, People's Republic of China
[3] Center for Astrophysics | Harvard & Smithsonian, 60 Garden Street, Cambridge, MA 02138, USA
[4] Fakultät für Physik und Astronomie, Julius-Maximilians-Universität Würzburg, Emil-Fischer-Str. 31, 97074 Würzburg, Germany
[5] Anton Pannekoek Institute for Astronomy & GRAPPA, University of Amsterdam, Science Park 904, 1098 XH Amsterdam, The Netherlands
[6] INAF Istituto di Astrofisica e Planetologia Spaziali, Via del Fosso del Cavaliere 100, 00133 Roma, Italy
[7] National Radio Astronomy Observatory, 520 Edgemont Road, Charlottesville, VA 22903, USA
[8] South African Radio Astronomy Observatory, 2 Fir Street, Cape Town, 7925, South Africa
[9] INAF Osservatorio Astrofisico di Arcetri, Largo Enrico Fermi 5, 50125 Firenze, Italy
[10] Dipartimento di Fisica e Astronomia, Università degli Studi di Firenze, Via Sansone 1, 50019 Sesto Fiorentino (FI), Italy
[11] Istituto Nazionale di Fisica Nucleare, Sezione di Firenze, Via Sansone 1, 50019 Sesto Fiorentino (FI), Italy
[12] Graduate Institute of Astronomy, National Central University, 300 Zhongda Road, Zhongli, Taoyuan 32001, Taiwan
[13] Laboratory for Space Research, The University of Hong Kong, Cyberport 4, Hong Kong
[14] Istituto Nazionale di Fisica Nucleare, Sezione di Pisa, Largo B. Pontecorvo 3, 56127 Pisa, Italy
[15] Science and Technology Institute, Universities Space Research Association, Huntsville, AL 35805, USA
[16] NASA Marshall Space Flight Center, Huntsville, AL 35812, USA
[17] Department of Physics, The University of Hong Kong, Pokfulam, Hong Kong
[18] Instituto de Astronomía y Física del Espacio (IAFE), Av. Int. Guiraldes 2620, Pabellón IAFE, Ciudad Universitaria, 1428 Ciudad Autónoma de Buenos Aires, Argentina
[19] Department of Physics, Furman University, Greenville, SC 29613, USA
Received 2025 March 21; revised 2025 May 5; accepted 2025 May 5; published 2025 June 19

Abstract

We report the detection of a spatial variation of X-ray polarization in the southwestern (SW) shell of supernova remnant SN 1006 (SN 1006 SW) using the Imaging X-ray Polarimetry Explorer (IXPE). The shell has an average X-ray polarization degree (PD) of 21.6% ± 4.5% and polarization angle of −48° ± 5° in the 2–4 keV energy band, similar to those in the northeastern shell. The PD varies along SN 1006 SW, with a peak PD = 40% ± 8% in the south and a significantly lower PD $\lesssim$ 27% (99% upper limit) in the west, where the shell has been proposed to be interacting with an interstellar cloud. The correlation between the PD, which reflects the magnetic orderliness, and the preshock density provides observational evidence that magnetic turbulence and amplification are environment-dependent. The high PD detected in the southern region of the shell constrains the magnetic turbulence scale to $\lesssim$0.1 pc. Moreover, by comparing the IXPE X-ray and MeerKAT radio polarization measurements for SN 1006 SW, we found that magnetic fields traced by X-ray polarization are nearly radially distributed, whereas those traced by radio polarization tend to follow a direction parallel to the Galactic plane. This suggests that the X-ray polarization probes freshly amplified magnetic fields from small-scale structures in the immediate postshock region, while the radio traces more extended regions influenced by the preexisting ambient magnetic fields.

Unified Astronomy Thesaurus concepts: Supernova remnants (1667); Polarimetry (1278); Cosmic rays (329); Shocks (2086); Magnetic fields (994)

1. Introduction

Supernova remnants (SNRs) influence almost every component of the interstellar medium (ISM), which consists of gas, dust, cosmic rays (CRs), magnetic fields, and radiation (B. T. Draine 2011). While driving shocks into the gas, they accelerate particles to the relativistic regimes (a.k.a. CRs) and strongly modify magnetic fields. Shocks, magnetic fields, and CR acceleration processes are closely coupled—we cannot fully understand one process without considering how it interacts with the others. A crucial open question is whether SNRs can accelerate CRs to the PeV energy regime. For SNRs to behave as PeVatrons, the magnetic field needs to be highly amplified to keep CRs being accelerated near the shock (see the review by P. Blasi 2013).

X-ray observations have demonstrated that magnetic fields can be amplified by a factor of 10–100 in young SNRs (J. Vink & J. M. Laming 2003; E. Parizot et al. 2006; Y. Uchiyama et al. 2007). However, the mechanism behind magnetic field amplification in SNRs remains poorly understood. Potential mechanisms involve CR-driven instability (A. R. Bell 2004) and turbulent dynamo processes (e.g., T. Inoue et al. 2013; S. Xu & A. Lazarian 2017).

Polarization measurements unveil the magnetic field orientation and turbulence level through the electric vector

polarization angle (PA; perpendicular to the magnetic field orientation) and polarization degree (PD), respectively, and thus provide insight into this question. Radio polarimetry of SNRs has been conducted for decades (see references within the review by G. Dubner & E. Giacani 2015), whereas X-ray imaging polarization became possible only recently, starting in 2021 with the launch of the Imaging X-ray Polarimetry Explorer (IXPE; M. C. Weisskopf et al. 2022).

IXPE has observed six SNRs to date, providing new knowledge of magnetic fields close to the shock front of young SNRs, some discoveries of which were unexpected (see a recent review by P. Slane et al. 2024). Three SNRs observed in the first year of IXPE are Cas A, Tycho, and SN 1006 (G327.6+14.6, NE shell). They show different PD in the rim from 4.5% ± 1.0%, 12% ± 2% to 22.4% ± 3.5% (J. Vink et al. 2022; R. Ferrazzoli et al. 2023; P. Zhou et al. 2023). Although all three of these young SNRs reveal X-ray PA tangential to the shell (corresponding to radially oriented magnetic fields), later IXPE observations of RX J1713.3-3946 (R. Ferrazzoli et al. 2024) and Vela Jr. (D. A. Prokhorov et al. 2024) unexpectedly revealed X-ray PAs perpendicular to the shell, supporting a compression origin of the magnetic fields even for these dynamically young SNRs. Another interesting finding seen so far is that none of these SNRs share similar PD. The reason is unclear but might be related to the environmental density and magnetic field, shock velocity, SNR age, and whether IXPE can resolve the magnetic turbulence scale (P. Slane et al. 2024). Other possibilities, such as the ion-neutral damping when CR currents interact with neutrals, might also change the magnetic turbulence level and, thus, the PD (L. O'C Drury et al. 1996).

To examine the influence of ambient density on magnetic turbulence, a viable way is to perform imaging polarimetry of an individual SNR and measure how the polarization properties change as ambient density varies along the rim. This motivated us to observe the southwestern (SW) shell of SN 1006 with IXPE (see Figure 1). The western part of the shell is proposed to interact with an atomic cloud, but the SW part of the shell is expanding in a low-density medium (G. M. Dubner et al. 2002; M. Miceli et al. 2014).

Another motivation for observing SN 1006 SW is to explore whether X-ray and radio polarization properties have large differences. For SNRs, no direct comparison of PA between X-ray and radio bands has been made. SN 1006 provides a particularly appropriate case for such an investigation, because its large angular size (30′) enables a detailed spatially resolved polarimetric analysis of the shell. Moreover, the high-resolution MeerKAT radio polarimetric data are available for direct comparison with the X-ray polarization data. The X-ray and radio polarization measurements will help to reveal the magnetic field properties in the immediate and far postshock regions, respectively, since the electrons at the X-ray bands have a short synchrotron cooling timescale. Radio polarization observations show that a large fraction of the magnetic fields in SN 1006 lie parallel to the Galactic plane, although there is also a radial component (E. M. Reynoso et al. 2013; W. D. Cotton et al. 2024). The origin of the two components needs further study.

2. Data

2.1. IXPE Observations

IXPE observed the SW shell of SN 1006 (see Figure 1) in six epochs between 2024 February 3 and March 18, providing a total exposure time of 988 ks. The photon rate in the observations was stable except for an enhanced flux in a small fraction of time due to contamination from a solar flare. We determined the good time intervals with a 3σ clipping for the 2–8 keV lightcurve to remove flares with anomalously high count rates. This filtered out 2/12.4/4.5 ks from the data of detector units 1/2/3.

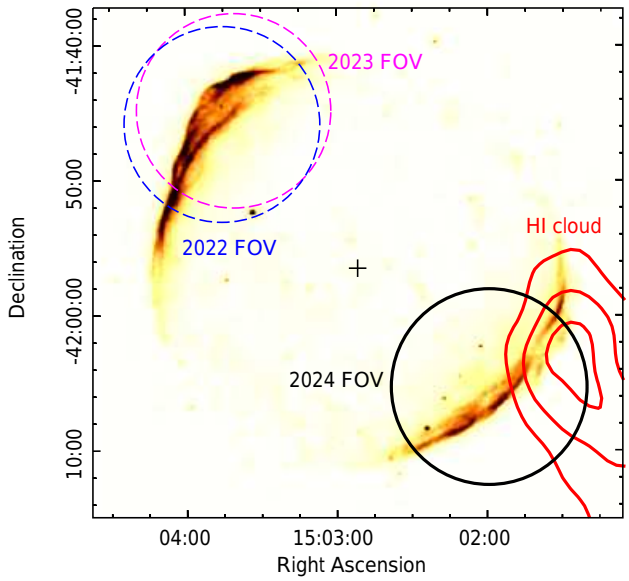

Figure 1. FOV of the IXPE observations overlaid on the XMM-Newton 2–8 keV image of SN 1006 (J.-T. Li et al. 2016). The solid and dashed circles denote the FOVs for the current observation of SN 1006 SW and previous observations of SN 1006 NE. The red contours show the H I intensity integrated within the local standard of rest velocity interval of 5.7–10.7 km s^{-1}. The plus sign shows the SNR center ($15^h02^m51\overset{s}{.}7$, $-41°56'33''$ J2000; S. P. Reynolds & D. M. Gilmore 1986; P. F. Winkler & K. S. Long 1997).

The software `ixpeobssim` version 31.0.1 (L. Baldini et al. 2022) was used to reduce and analyze the IXPE data. Specifically, we used `PCUBEMAP` and `PCUBE` algorithms in the `xpbin` command to generate polarization images and extract Stokes parameters in spatial regions, respectively. We applied the `Xselect` and `Xspec` packages (version 12.14.0b) in the `HEASoft` software for spectral extraction and analysis. The spectra were weighted using the NEFF method, and the weighted response files of each region were generated using the `ixpecalcarf` command.[20] The Stokes I spectra were grouped to reach at least 50 counts per bin. For the Stokes Q and U spectra, we used a constant 0.4 keV energy binning.

To reduce the instrumental background, we adopted an energy-dependent background rejection method described in A. Di Marco et al. (2023). Although this method removes about 40% of the instrumental background, the remaining background still dominates over the sky X-ray background in the region of SN 1006. Therefore, background subtraction was conducted in the analysis for source regions. We used the IXPE 2–4 keV band for polarization analysis throughout the paper in order to maximize the signal-to-background ratio. This band was also used for the previous study of SN 1006 NE (P. Zhou et al. 2023).

[20] https://heasarc.gsfc.nasa.gov/docs/ixpe/analysis/ixpe_quickstart.pdf

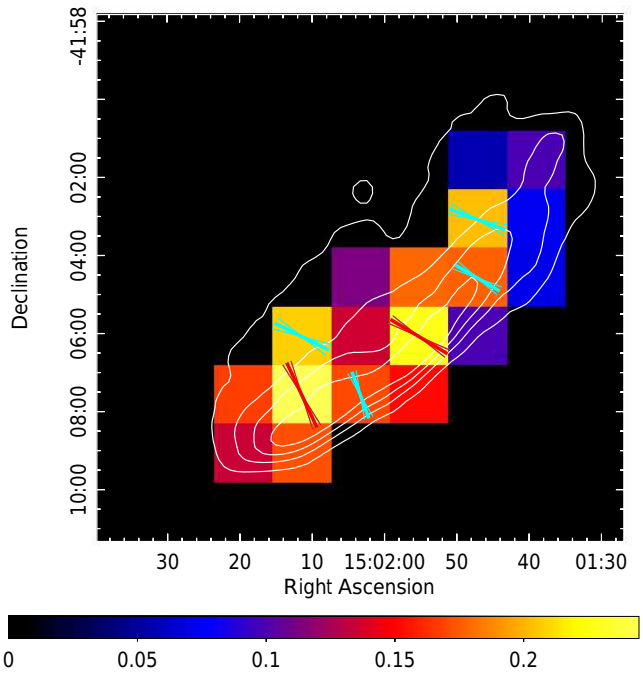

Figure 2. X-ray PD overlaid with Stokes I contours and magnetic vectors (with 1σ error). Only pixels with Stokes I values larger than 175 are shown. The pixel size is 1.″5 and the energy band is 2–4 keV. The red and cyan vectors denote the pixels with $>3\sigma$ and 2σ–3σ detection, respectively.

Similar to the observations of the NE shell, there was also an offset of the IXPE pointing due to difficulties in correcting imaging effects from dynamical bending of the telescope boom using only extended sources (J. Vink et al. 2022). IXPE detected a point source in the field of view (FOV), but its position is misaligned with that observed in the Chandra observation taken in 2012 ($15^{h}02^{m}03\overset{s}{.}4$[, $-42°02'19\overset{''}{.}7$, J2000). To correct the offset, we matched the positions of the point source in the IXPE and Chandra images and obtained the corrected reference coordinates of the IXPE data ($15^{h}01^{m}59\overset{s}{.}3$, $-42°05'20\overset{''}{.}0$, J2000).

2.2. Chandra X-Ray and MeerKAT Radio Data

We retrieved three archival Chandra/ACIS-I X-ray observations toward the west and SW of SN 1006 (obsIDs: 13738, 13739, and 14424), contained in the Chandra Data Collection doi:10.25574/cdc.372. These observations were conducted between 2012 April 23 and May 4, with a total exposure of 199 ks. We used CIAO software to reduce the data and `Xspec` to analyze the spectra. The main usages of the Chandra observations include image comparison with IXPE and X-ray spectral analysis. The latter constrains the absorption of X-ray emission by the foreground ISM (see Section 3.2 for details).

To compare the polarization between X-ray and radio bands, we used MeerKAT L-band (856–1712 MHz) polarization images, which have an angular resolution of 7.″5 (W. D. Cotton et al. 2024). The MeerKAT data have been corrected for the intervening Galactic Faraday rotation.

3. Results

3.1. Distribution of Polarization Parameters

Figure 2 shows the PD and magnetic field distribution of SN 1006 SW rim in the 2–4 keV band for a pixel size of 1.″5. We obtained PD and PA from the Stokes I, Q, and U values in each pixel: $\mathrm{PD}=\sqrt{Q^2+U^2}/I$, $\mathrm{PA}=0.5\arctan(U/Q)$ (measured on the plane of the sky from north to east; International Astronomical Union standard). Two of these pixels show PD = 23%–24% with a $>3\sigma$ significance (red vectors, PD error of 6%), and four pixels have PD = 17–21% with a 2σ–3σ significance (cyan vectors, PD error of 6%–8%). The PA values range between $-20°$ and $-70°$ with an uncertainty of 7°–12°. The magnetic vectors are nearly perpendicular to the shell, suggesting a radial magnetic field distribution. In Appendix A, we show the polarization maps resulting from Gaussian smoothing, which produces a consistent distribution. We note that the significance mentioned above is a pre-trial value, not corrected for the number of pixels. Moreover, the IXPE emission of SN 1006 SW is contaminated by a nonnegligible level of instrumental background. This background needs to be removed to restore the true polarization parameters of SN 1006 SW.

We thus extracted X-ray polarization parameters from regions of interest as labeled in Figure 3, with background evaluated from the emission-free regions away from the shell. The PD, PA, and polarization significance are listed in Table 1. The polar plots of PD, PA, and their confidence levels are shown in Figure 8 in Appendix A.

A large background region is necessary to enhance the statistical quality of polarization parameters. Therefore, we used a large background area "bkg" that covers two regions in the SW and NE (in the SNR interior). Weak thermal emission exists in the SNR interior below 2 keV (J.-T. Li et al. 2016), but our polarization analysis focuses on 2–4 keV. Moreover, we found that the NE portion of "bkg" (see Figure 3) is only ∼13% brighter than in the SW in 2–4 keV, meaning that SNR contribution is subdominant in the "bkg" NE region. The X-ray emission from the "bkg" region is consistent with being unpolarized with PD(bkg)<9.2% at 99% confidence level.

We selected "SWshell" for the entire SW shell, including both the bright rim and the faint part. We detected polarization in this region at a 4.8σ level and obtained $\mathrm{PD}=21.6\%\pm4.5\%$ and $\mathrm{PA}=-48°\pm5°$. These numbers are close to the values in the NE shell: $\mathrm{PD(NE)}=22.4\%\pm3.5\%$ and $\mathrm{PA(NE)}=-45°\pm4°$ (P. Zhou et al. 2023).

To explore the polarization variation along the radial direction, we defined regions "layer1," "layer2," and "layer3" from the bright rim to the areas behind the shock. The former two regions have PD values of 26% ± 5%, 28% ± 8% (1σ error), respectively, while the 99% upper limit of PD in "layer3" is 80.8%. Considering the error range, the current data do not reveal a significant change in polarization along the radial direction.

We found a variation of PD and PA along the azimuthal regions "J," "K," "L," and "M." The PD is largest in "J" ($\mathrm{PD(J)}=40\%\pm7\%$), with a high significance of 5.7σ, but reduced at its neighboring region "K" ($\mathrm{PD(J)}=22\%\pm7\%$)). "M" corresponds to the region impacted by a H I cloud, where PD(M) < 29.0% at a confidence level of 99%. Moreover, the PA presents an increasing trend from $\mathrm{PA(J)}=-68°\pm4°$ to $\mathrm{PA(L)}=-34°\pm7°$. The difference in PA is significant between these two regions, at a 4.2σ level, suggesting that PA in SN 1006 is not perfectly parallel, but varies along the azimuthal angles.

To verify whether PA in SN 1006 SW aligns along the shell direction, we reconstruct the event files based on the circular

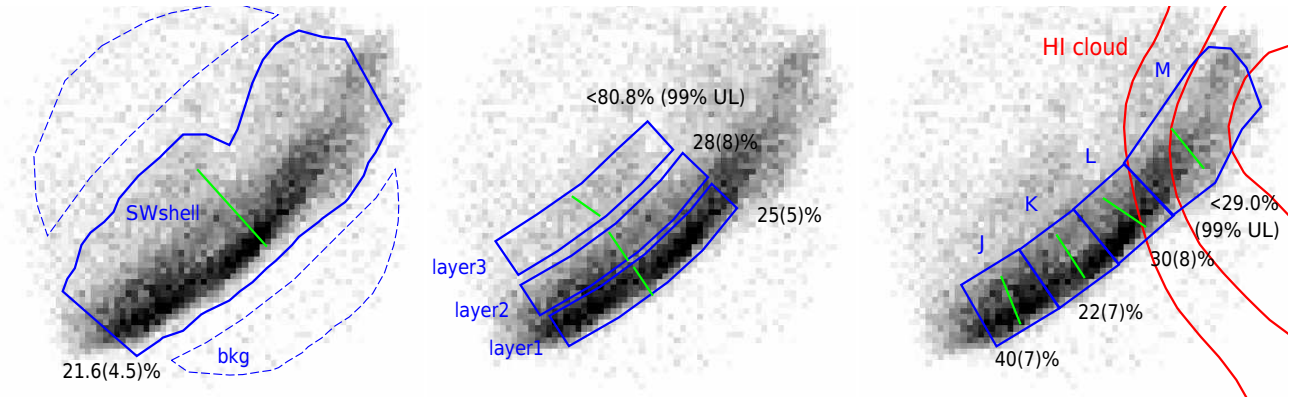

Figure 3. Regions selected in our polarization analysis on top of Stokes I images. The dashed regions show the background area. The PD (with its 1σ error or 99% upper limit) is labeled beside each region, and the mean PA values are shown with green lines (see the polarimetric results in Table 1). The position of the H I cloud is identified by the red contours, reflecting the H I flux between 5.7 and 10.7 km s^{-1}. The H I data are taken from G. M. Dubner et al. (2002).

Table 1
Polarization Results of Eight Regions by IXPE and MeerKAT Observations

Region	IXPE (Polarimetric)			IXPE (Spectropolarimetric)			Radio	
	PD (%)	PA (°)	σ	PD (%)	PA (°)	Γ	PA_r (°)	PA_r–PA (°)
SWshell	21.6 ± 4.5	−48 ± 5	4.8	21.5 ± 4.7	−47 ± 6	2.81 ± 0.05	−28.9 ± 0.3	19 ± 5
Layer1	24.6 ± 5.3	−56 ± 6	4.6	33.2 ± 5.8	−53 ± 5	2.74 ± 0.06	−32.6 ± 0.8	23 ± 6
Layer2	28.1 ± 7.7	−56 ± 7	3.6	26.9 ± 8.3	−53 ± 10	3.00 ± 0.09	−30.2 ± 0.6	26 ± 7
Layer3	<80.8	⋯	2.1	<75.5	⋯	3.16 ± 0.18	−30.4 ± 0.7	⋯
J	40.0 ± 7.0	−68 ± 4	5.7	40.0 ± 7.7	−67 ± 5	2.79 ± 0.08	−28.2 ± 0.8	40 ± 4
K	21.6 ± 7.3	−57 ± 9	3.0	27.6 ± 8.0	−55 ± 9	2.83 ± 0.08	−30.5 ± 0.8	27 ± 9
L	29.8 ± 7.6	−34 ± 7	3.9	35.3 ± 8.5	−38 ± 7	2.92 ± 0.09	−35.8 ± 0.8	−1 ± 7
M	<29.0	⋯	2.1	<26.6	⋯	2.67 ± 0.08	−21.9 ± 0.8	⋯

Note. The regions are denoted in Figure 3. The polarization results are obtained using the 2–4 keV data. The errors are provided at the 1σ confidence level, except for regions Layer3 and M, with low significance, we give 99% upper limits for the PD values.

polarization geometry model using the `xpstokesalign` command in `ixpeobssim`. All the Stokes Q and U parameters of each event are rotated with respect to the SNR center at R.A. (J2000) = $15^h02^m51\overset{s}{.}7$, decl. (J2000) = $-41°56'33''$ (S. P. Reynolds & D. M. Gilmore 1986; P. F. Winkler & K. S. Long 1997), so that we would find the reconstructed PA of 0° if the initial PA aligns with the shell. With the aligned data, we found PA_{align} of 0° ± 5° in region "SWshell", and −11° ± 5°, −9° ± 9°, −6° ± 7°, and −19° ± 14° for regions "J," "K," "L," and "M," respectively. This supports the finding that PA in SN 1006 SW is tangential to the shell, and the magnetic fields are radially distributed.

3.2. Spectropolarimetric Analysis

We performed spectropolarimetric analysis for the regions as shown in Figure 3. This analysis has some advantages compared to the pure polarimetric method (`PCUBE`). First, it allows simultaneous measurements of spectral and polarization parameters, with a correction for the vignetting effect. Moreover, it can provide the (posterior) probability distribution of PD and PA, and thus allows a more reliable comparison of PD or PA between regions.

We extracted weighted Stokes I, Q, and U spectra from these regions and subtracted the background Stokes spectra. These spectra in 2–4 keV were then fitted using an absorbed power-law model with a constant polarization: `tbabs*polconst*powerlaw` in `Xspec` (see Figure 4 for region "SWshell"). We adopted solar abundance from M. Asplund et al. (2009) and the Tuebingen-Boulder ISM absorption model `tbabs`, which calculates the cross section for X-ray absorption by multiphase gas and dust. The spectra of SN 1006 in the IXPE 2–4 keV energy band are not sensitive to the absorption parameter, i.e., equivalent atomic column density N_H, because spectra above 2 keV are not affected by the moderate column densities toward SN 1006. Therefore, we fitted a 1–8 keV Chandra X-ray spectrum in "SWshell" region with the `tbabs*powerlaw` model and obtained $N_H = 3.27 \pm 0.02 \times 10^{21}$ cm^{-3}. This best-fit value is then used and fixed for the IXPE spectral fitting.

We applied the Markov Chain Monte Carlo (MCMC) method (D. J. C. Mackay 2003) to provide the mean values and error ranges of parameters. We use the Goodman–Weare algorithm (J. Goodman & J. Weare 2010) with 20 walkers and a total length of 200,000, with the first 100,000 steps discarded. After reaching equilibrium, the MCMC chains can be converted to posterior probability distributions of parameters, and thus provide parameter error ranges as tabulated in Table 1. The PD and PA values from this spectropolarimetric approach are consistent with the polarimetric results within the error range.

The spectropolarimetric results demonstrate a variation of X-ray PD along the shell: The MCMC chains provide the posterior probability distributions of PDs in regions and the combined region "JKL" (PD(JKL) = 31.7% ± 4.6%; see Figures 9 and 10 in Appendix A). The probability is 99.56% and 99.83% for PD(JKL) > PD(M) and PD(J) > PD(M),

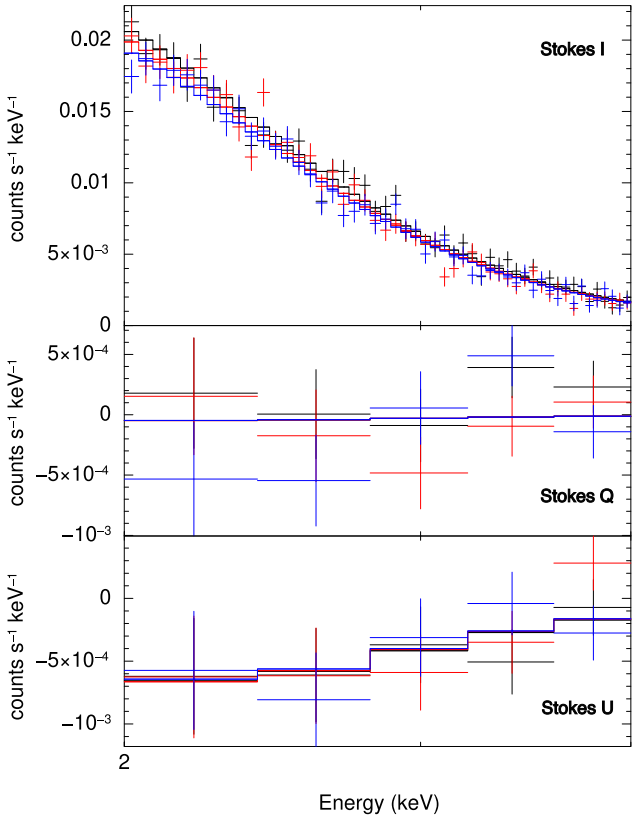

Figure 4. Stokes I, Q, and U spectra of region "SWshell" fitted using the `tbabs * polconst * powerlaw` model. The black, red, and blue data are extracted from DU 1, 2, and 3, respectively.

respectively. Using χ^2 statistics to fit the spectra results in a consistent probability of 99.41% for PD(JKL) > PD(M) (see Appendix B).

3.3. Radio PA

Radio and X-ray synchrotron emissions are radiated by electrons of different energies and lifetimes, with radio emission arising typically from 10^8 to 10^{10} eV electrons, and X-ray synchrotron emission from typically 10^{13}–10^{14} eV electrons. Therefore, it is of interest to investigate whether the polarization properties of these two bands are the same. In this paper, we only compare PA values, given that the missing flux issue in the radio interferometric observations with MeerKAT makes a reliable radio PD measurement difficult (see W. D. Cotton et al. 2024 for a detailed explanation). From the MeerKAT L-band polarization data, we obtained PA values in the eight regions and listed them in Table 1. The MeerKAT data have a finer angular resolution of 7.″5 than IXPE. To compare these two data, we first smooth the MeerKAT polarization images to reach an angular resolution of 30″.

The radio PA values (PA_r) in each region are calculated using the polarized flux (PF) and PA images:

$$\begin{aligned} PA_r &= 0.5 \arctan \frac{\sum U_i}{\sum Q_i} \\ &= 0.5 \arctan \frac{\sum PF_i \sin(2PA_i)}{\sum PF_i \cos(2PA_i)}, \end{aligned} \quad (1)$$

where the subscript i means the ith pixel.

The radio PA_r values in all regions are around −30° (see Table 1), except for the region "M" that has a slightly larger PA_r of −22°. This deviates significantly from the X-ray PA results. At the region "SWshell", the radio $PA_r = -28.9^\circ \pm 0.3^\circ$ differs from the X-ray PA$= -48^\circ \pm 5^\circ$ at the 3.8σ level. The discrepancy is most prominent in the region "J," which has PA$-PA_r \approx 40^\circ$ (9.8σ). Therefore, the X-ray and radio polarization, or the magnetic fields traced by these two bands, have large differences.

4. Discussion

4.1. A Variation in X-Ray PD along the Shell

We have found a significant variation in X-ray PD along SN 1006 SW (see Sections 3.1 and 3.2), with a peak PD of 40% ± 8% in the southern region "J" and a low PD of <27% (99% upper limit) in the western region "M" (see the regions in Figure 3). This suggests that the magnetic field is quite ordered in the eastern part of the SW shell (high PD), but is more randomly distributed in the west (low PD), where the SNR is suggested to interact with an atomic cloud (G. M. Dubner et al. 2002; M. Miceli et al. 2014). The cloud spatially corresponds to an X-ray-dim area (see Figure 1), which can be attributed to a lower cutoff energy of the X-ray synchrotron emission in that region (M. Miceli et al. 2014). M. Miceli et al. (2014) estimated the atomic gas density to be 9–16 cm^{-3} from the H I observations, and the cloud must be partially in front of SN 1006, as the X-ray absorption column is larger in that region. One might expect enhanced thermal X-ray emission in those regions in which the shell interacts with the dense cloud. This is not observed, which puts some constraint on the density of the postshock gas, which depends on the assumed electron temperature. M. Miceli et al. (2014) estimated postshock gas densities of <12, 3, 0.3 cm^{-3}, for electron temperatures of 0.05, 0.25, and 2 keV, respectively. Since the shell is at the edge of the atomic cloud, the local density may be lower than the 9–16 cm^{-3} inferred for the atomic cloud. But the postshock density must be higher than around the rest of the shell of SN 1006, which has been estimated to be 0.16–0.34 cm^{-3} (F. Acero et al. 2007; S. Katsuda et al. 2009; M. Miceli et al. 2014; R. Giuffrida et al. 2022).

In region "J" with fairly ordered magnetic fields, the magnetic turbulence scale $l_{\Delta B}$ is inferred from the scale of its X-ray structure. Since the X-ray photons mainly come from the bright rim, the magnetic turbulence scale is likely similar to or slightly smaller than the rim thickness (11″ S. M. Ressler et al. 2014), ∼0.1 pc at region "J" for an SNR distance of 2.18 kpc (P. F. Winkler et al. 2003). At region "M," the lower PD indicates a depolarization due to a smaller turbulence scale.

Here we discuss two possible scenarios that may explain the decreased PD at the shock-cloud interaction region: instability caused by density fluctuation of the ISM and instability induced by CRs.

First, when a shock propagates through an inhomogeneous ISM, it triggers plasma instability, leading to magnetic turbulence with a characteristic scale proportional to the length scale of the density dispersion (T. Inoue et al. 2013; S. Xu & A. Lazarian 2017). This mechanism is expected to occur in Cas A, which shows a low X-ray PD in the rim (4.5% ± 1.0%; J. Vink et al. 2022) since this young SNR is evolving in a highly clumpy circumstellar medium

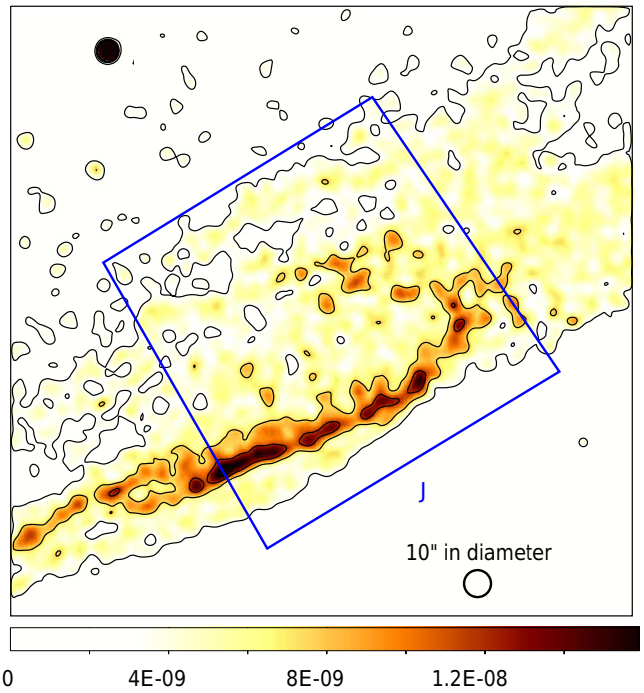

Figure 5. Clumpy structures of the synchrotron emission in the SW shell of SN 1006 revealed with Chandra 2–8 keV flux image (in units of count s^{-1} cm^{-2}). The image with a pixel size of 0.″49 is smoothed with a Gaussian kernel (σ) of 4 pixels. The blue box shows the region "J" and the black circle marks a scale of 10″ (~0.1 pc).

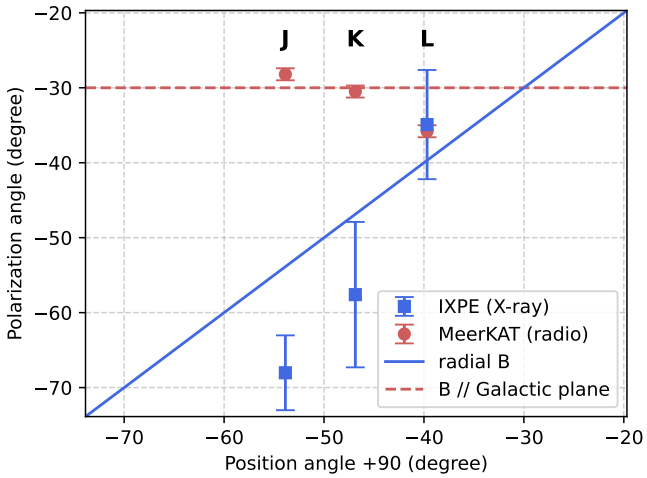

Figure 6. PAs measured in three regions with IXPE and MeerKAT compared to the position angles (+90°, with 0° to the north) of the regions. The solid and dashed lines represent two magnetic configurations, radial magnetic orientation and magnetic fields parallel to the Galactic plane, respectively. The error bars show the 1σ range.

(J. Vink et al. 1996; R. A. Chevalier & J. Oishi 2003; B.-C. Koo et al. 2023). Tycho, with a PD of 12% ± 2% (R. Ferrazzoli et al. 2023), is also likely to experience some level of magnetic turbulence due to its nonuniform ambient medium (B. J. Williams et al. 2013; P. Zhou et al. 2016; T. Tanaka et al. 2021). In SN 1006 SW, the density of the atomic cloud close to region "M" is two orders of magnitudes larger than the average value near SN 1006 (0.04–0.85 cm^{-3}, F. Acero et al. 2007; S. Katsuda et al. 2009; R. Giuffrida et al. 2022), providing an inhomogeneous condition that may generate small-scale magnetic turbulence. In contrast, the PD reaches 40% at the southern region "J," where the shell is expanding into a low-density medium. Therefore, density fluctuation is unlikely to play a significant role in driving magnetic turbulence at region "J."

The alternative explanation involves the streaming instability of CR currents, which causes strong amplification and turbulence of magnetic fields in the shock upstream (A. R. Bell 2004). This instability also generates plasma fluctuations and thus ripples the shock surface, triggering plasma and magnetic turbulence downstream (D. Caprioli & A. Spitkovsky 2014; A. M. Bykov et al. 2024).

The length scale of Bell instability in the preshock inversely scales with the ambient density $l_{\rm Bell} \propto n_0^{-1} V_s^{-3} E_{\rm max} B_0 \propto n_0^{-1}$, where V_s, $E_{\rm max}$, and B_0 are the shock speed, maximum energy of the CRs, and the ambient magnetic strength. Assuming a similar turbulence scale between the preshock and postshock, we estimate $l_{\rm Bell} \sim l_{\Delta B} \sim 0.1$ pc at region "J." This would indicate a nonuniform X-ray brightness at this scale, which is found in the Chandra X-ray image as shown in Figure 5. In the high-density region with an atomic cloud, the Bell instability occurs on a smaller scale. For example, assuming $n_0 = 0.05\,{\rm cm}^{-3}$ near region "J" and $= 0.5\,{\rm cm}^{-3}$ near region "M" (cloud density is 9–16 cm^{-3} M. Miceli et al. 2014), $l_{\rm Bell}$ is expected to be 10 times smaller in region "M." Therefore, the depolarization can explain the lower PD found in the region "M". We note that the shock velocity, $E_{\rm max}$, and B_0 may also be different between regions in SN 1006 SW, but these values are unknown so far.

4.2. Large Difference between the X-Ray and Radio PA

The large discrepancy between the X-ray and radio PA (see Table 1) constitutes strong evidence that the magnetic fields traced by these two bands are not the same. We notice that the magnetic orientation is predominantly radial as revealed by the X-ray polarization, while consistent with the direction of the Galactic plane (~60°, for $PA_r \sim -30°$) as probed by the radio emission (see Figure 6).

As shown in Figure 6, X-ray PA values increase with the position angle of the regions from −144° ± 4° in the region "J" to −130° ± 5° in region "L" (with 0° to the north). The difference between PA and position angle +90° is within ~14° for the three regions with significant polarization detection. This correlation supports the idea that X-ray emission is generated in an area with predominantly radial magnetic fields. There is also a tiny deviation from the perfectly radial distribution, which may be real or due to the random error of the measurement. Moreover, the overall X-ray PA in SN 1006 SW and SN 1006 NE can be described with a tangential model, with $PA_{\rm align}$(SWshell) = 0° ± 5° (see Section 3.1) and $PA_{\rm align}$(NEshell) = 1° ± 5° (P. Zhou et al. 2023).

We also calculated the MeerKAT PA for the NE shell of SN 1006: PA = −36° ± 0.°8, −32.°2 ± 0.°8 , and −27.°0 ± 0.°7 for regions "A," "B," and "C" (see regions in Figure 3 of P. Zhou et al. 2023), respectively. The corresponding IXPE X-ray PA values are −49.°5 ± 6.°2 and −43.°7± 6.°2, and −40.°0 ± 8.°3. Using the χ^2 test ($\chi^2 = \sum_i \frac{[{\rm PA}(i) - {\rm PA}_r(i)]^2}{{\rm var}[{\rm PA(i)} - {\rm PA}_r[i)]} = 10.76$, i for regions "A," "B," and "C"), the X-ray and radio PA values are different at the 99% confidence level, less significant than in SN 1006 SW.

The radial magnetic field orientation in SN 1006 revealed with IXPE is inconsistent with the compression origin of the magnetic fields. This is because shock compression of the

interstellar magnetic fields can amplify the tangential component in the postshock, while the radial component remains unaffected, resulting in tangentially distributed magnetic fields. The radially distributed magnetic fields have been observed in two younger SNRs, Cas A and Tycho, and the NE shell of SN 1006. An explanation of this orientation is the stretching of turbulent magnetic fields along the shock direction (see J. Vink et al. 2022; R. Ferrazzoli et al. 2023; P. Zhou et al. 2023, for details).

Hereafter, we discuss the physical origins of the different magnetic field configurations revealed by X-ray and radio polarimetry. First, the X-ray and radio emission comes from different regions. The characteristic electron cooling timescale in the magnetic field B is $\tau_{\rm cool} = 634/(B^2E)$ s (e.g., S. P. Reynolds 1998; J. Vink 2020). The very-high-energy electrons that produce X-ray emission cool faster, and thus, the X-ray emission traces regions closer to the particle acceleration sites, while the lower-energy electrons that give rise to the radio emission would have a broader distribution in the postshock region. The width of the X-ray synchrotron filament is determined by the advection length scale of the cooling electrons (J. Vink 2020): $l_{\rm adv} = \tau_{\rm cool}(V_{\rm s}/4) \approx 0.25\left(\frac{h\nu}{3\ \ {\rm keV}}\right)^{-1/2}\left(\frac{B}{30\ \ \mu G}\right)^{-1/2}\left(\frac{V_{\rm s}}{5000\ \ {\rm km\ s^{-1}}}\right){\rm pc}$, with $B \sim 30\,\mu$G (F. Acero et al. 2010; Y. Xing et al. 2016) and shock velocity $V_{\rm s} \sim 5000\,{\rm km\,s^{-1}}$ (P. F. Winkler et al. 2014). This corresponds to an angular width of $24''$, similar to the observed width of the X-ray filament in the SW shell. The radio synchrotron structures are more extended than the X-ray and have a larger depth along the line-of-sight.

Besides the electron distribution, the magnetic fields in the immediate postshock and the far postshock can also be different. The strong amplification of the turbulent magnetic fields happens at the immediate postshock and decays in the far postshock (A. M. Bykov et al. 2024). In the Bell instability scenario, the highly amplified magnetic fields downstream contain two layers, with a thin layer of compressed transverse magnetic fields followed by a wider layer of predominantly radial magnetic fields generated by a turbulent dynamo mechanism (A. M. Bykov et al. 2024). An alternative possibility is that small scale, strongly magnetized structures (such as filaments) that are unresolved at Chandra's resolution contribute to the X-ray emission. On the other hand, the radio emission is from both small-scale structures and more extended regions. Note that the synchrotron emissivity scales with magnetic field strength as $\propto B^{1+\Gamma}$. Since the radio spectral index is smaller ($\Gamma = \alpha + 1 \approx 1.6$; e.g., E. M. Reynoso et al. 2013) than in X-rays ($\Gamma \approx 2.8$), the X-ray emission is much more biased toward plasma with relatively large magnetic field strengths.

We have discussed two possible aspects that may lead to the PA difference: (1) X-rays come from regions closer to the shock than the radio; (2) X-rays come from regions with stronger magnetic fields. Aspect (1) alone has the problem of why the magnetic field in the far downstream would turn back to the Galactic value. We consider it likely that both of these effects contribute to the observed differences between the radio and X-ray PA values.

Therefore, our X-ray polarization measurement supports the hypothesis that the magnetic fields have a turbulent origin rather than a compression origin. The X-ray-probed magnetic component is a newly generated component whose energy is gained from the very-high-energy particles that are freshly accelerated. The coincidence between the radio-probed magnetic fields and the Galactic plane is also interesting, as it may suggest that CR-driven turbulence dissipates far downstream, leaving the Galactic background field dominant.

5. Conclusion

IXPE has observed both the NE (P. Zhou et al. 2023) and SW shells of SN 1006 (this paper). The X-ray PD and angle are $21.6\% \pm 4.5\%$ and $-48^\circ \pm 5^\circ$ in SN 1006 SW, similar to that in the NE, thus supporting an overall symmetry for the double limbs of the SNR.

Nevertheless, the new IXPE observations toward the SW shell reveal a variation of polarization properties along the shell. We detected a change in PD, which peaks in the south ($40\% \pm 7\%$) and decreases below $\sim$27% (99% upper limit) in the western shell impacted by a denser ambient medium. This reflects a correlation between enhanced magnetic turbulence and ambient gas density. We interpret that the decreased PD at region "M" results from either ISM-fluctuation-caused MHD instability or a smaller length scale of Bell instability.

The X-ray PA also varies along the shell and largely deviates from the radio PA. The magnetic fields probed by the X-ray band tend to follow a radial direction (along the shock normal) while those probed by the radio band follow the Galactic plane direction. We suggest that the X-ray polarization probes freshly amplified magnetic fields from small-scale structures in the immediate postshock, while the radio polarization is contributed by more extended regions. These results highlight the importance of X-ray polarimetry observations in studying magnetic fields and CR acceleration in SNRs.

Acknowledgments

We thank Dr. Gloria Dubner for kindly providing the H I data for SN 1006. We also thank Dawoon E. Kim for providing the scripts to plot polar plots of polarization parameters. IXPE is a joint US and Italian mission. The US contribution is supported by the National Aeronautics and Space Administration (NASA), led and managed by its Marshall Space Flight Center (MSFC), with industry partner Ball Aerospace (contract NNM15AA18C). The Italian contribution is supported by the Italian Space Agency (Agenzia Spaziale Italiana (ASI)) through contract ASI-OHBI-2017-12-I.0, agreements ASI-INAF-2017-12-H0 and ASI-INFN-2017.13-H0, and its Space Science Data Center (SSDC) and by the Istituto Nazionale di Astrofisica (INAF) and the Istituto Nazionale di Fisica Nucleare (INFN) in Italy. This research used data products provided by the IXPE Team (MSFC, SSDC, INAF, and INFN) and distributed with additional software tools by the High-Energy Astrophysics Science Archive Research Center (HEASARC) at NASA Goddard Space Flight Center (GSFC). P.Z. acknowledges the support from NSFC grant No. 12273010. P.S. acknowledges partial support from NASA Contract NAS8-03060. R.F., E.C., and P.S. are partially supported by MAECI with grant CN24GR08 "GRBAXP: Guangxi-Rome Bilateral Agreement for X-ray Polarimetry in Astrophysics." N.B. was supported by the INAF MiniGrant "PWNnumpol – Numerical Studies of Pulsar Wind Nebulae in The Light of IXPE." C.-Y.N. is supported by a GRF grant of the Hong Kong Government under HKU 17304524. E.M.R. is a member of the Carrera del

Investigador Científico of CONICET (Argentina) and is partially funded by CONICET grant PIP 11220220100211.

Facilities: IXPE, MeerKAT, CXO.

Software: `ixpeobssim` version 31.0.1 (L. Baldini et al. 2022), `DS9` (Smithsonian Astrophysical Observatory 2000; W. A. Joye & E. Mandel 2003), `Xspec` version 12.14.1 (K. A. Arnaud 1996), `Astropy` (Astropy Collaboration et al. 2013, 2018, 2022), `emcee` (D. Foreman-Mackey et al. 2013).

Appendix A
Polarization Map with Gaussian Smoothing

We applied a smoothing technique to produce the polarization map to improve the image statistics (D. A. Prokhorov et al. 2024). We first produce Stokes I, Q, and U and their variance maps with a pixel size of $8''$. Then, Stokes I, Q, and U images are smoothed with a Gaussian kernel of width $\sigma = 36''$ to produce PD and PA images as shown in Figure 7. The variances are smoothed with the kernel squared, and can be used to obtain polarization statistics per pixel, as $\chi^2_{2,i} = Q_i^2/\mathrm{var}(Q_i) + U_i^2/\mathrm{var}(U_i)$.

There are two "hot spots" along the rim with PD $\sim 25\%$, and peak significances of 5.2σ ($\chi^2_2 = 30.4$) and 5.0σ ($\chi^2_2 = 28.9$). The positions and values are similar to those in Figure 2, which is produced using a binning method (bin size of 1.′5). Therefore, the smoothing and binning methods provide consistent results. The polar plots of PD and PA of a few regions of interest (see Figure 3) are shown in Figure 8.

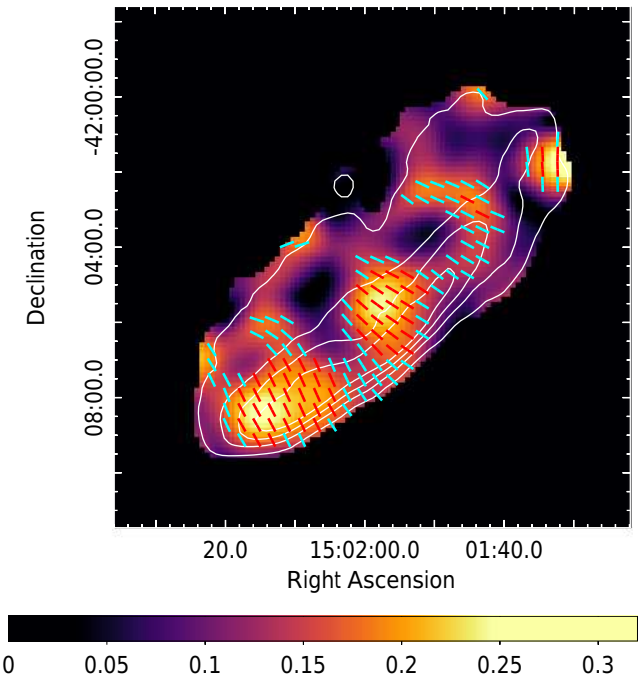

Figure 7. X-ray PD image resulting from smoothing the Stokes I, Q, and U with a Gaussian kernel of width $\sigma = 36''$. The Stokes I contours and magnetic vectors are overlaid. The significance is determined as explained in D. A. Prokhorov et al. (2024). Only for significant polarization detections are the vectors overlaid: red for over 3σ pixels and cyan for 2σ–3σ pixels.

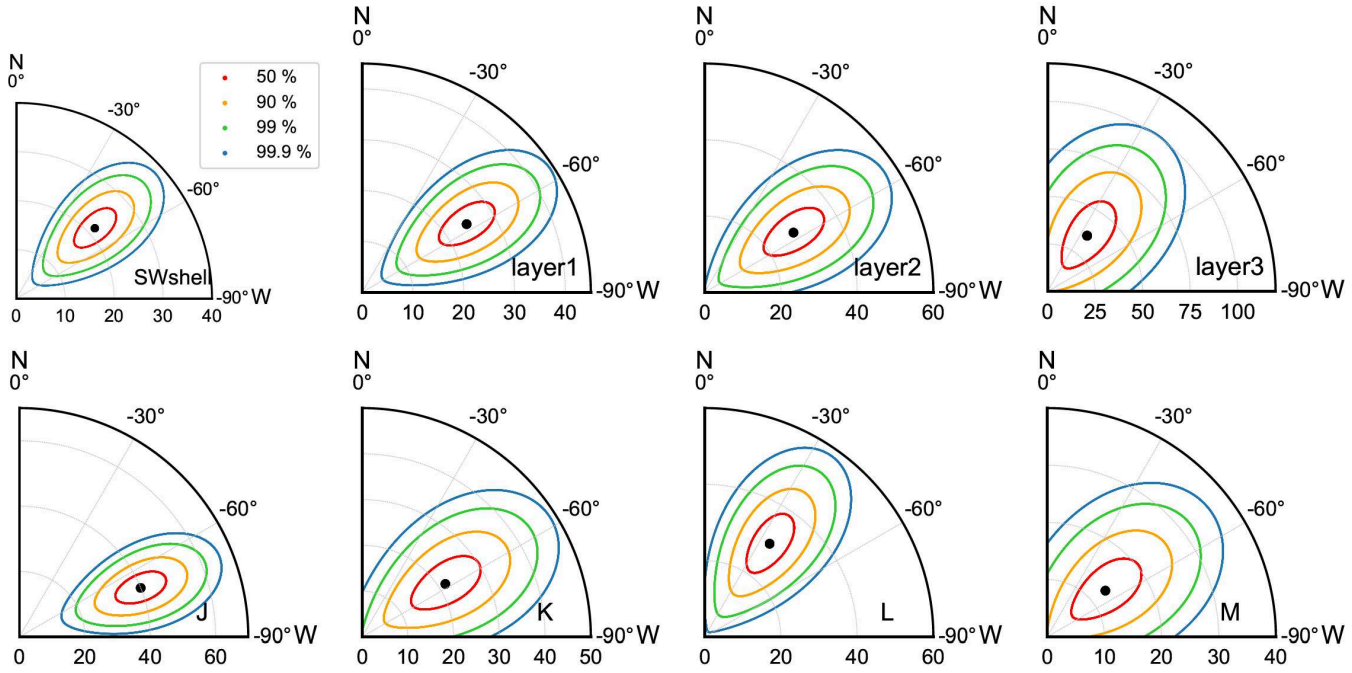

Figure 8. Polar plots of polarization parameters for regions in the 2–4 keV band (see regions in Figure 3). Each polar plot shows the PD (%) and PA in radial and position angle coordinates, respectively. The best-fit PD and PA values are denoted by black dots.

Appendix B
Comparison of PD between Regions Using MCMC Analysis and χ^2 Statistics

The MCMC analysis of spectropolarimetric data provides the posterior probability distribution for parameters in region "M" and the combined region "JKL." Figure 9 shows the two-dimensional correlation between parameters and the posterior distributions of individual parameters. In Figure 10, we compare the PD posterior probability distribution between region "JKL" and "M." The probability of PD(M) < PD(JKL) is derived as 99.56%.

In addition to the MCMC analysis, we also used the χ^2 statistic for the spectral fit to compare PD between regions "JKL" and "M." Using the `steppar` command, we calculated the χ^2 statistic value as a function of PD from 0.02 to 0.5 with a step of 0.02. The $\Delta\chi^2 = \chi^2 - \min(\chi^2)$ distribution can be converted to a probability distribution of PD. The probability of PD(M) < PD (JKL) is derived as $1 - \sum_{i=0}^{25}[\sum_{j=0}^{i} p_{\rm JKL}(j)]p_{\rm M}(i)$=99.41%, where $p_{\rm JKL}(i)$ is the probability of the real PD(JKL) value falling in the ith interval (intervals 0, 1, 24, and 25 correspond to PD = 0–0.02, 0.02–0.04, 0.48–0.5, and 0.5–1, respectively). This probability is consistent with that obtained from the MCMC method.

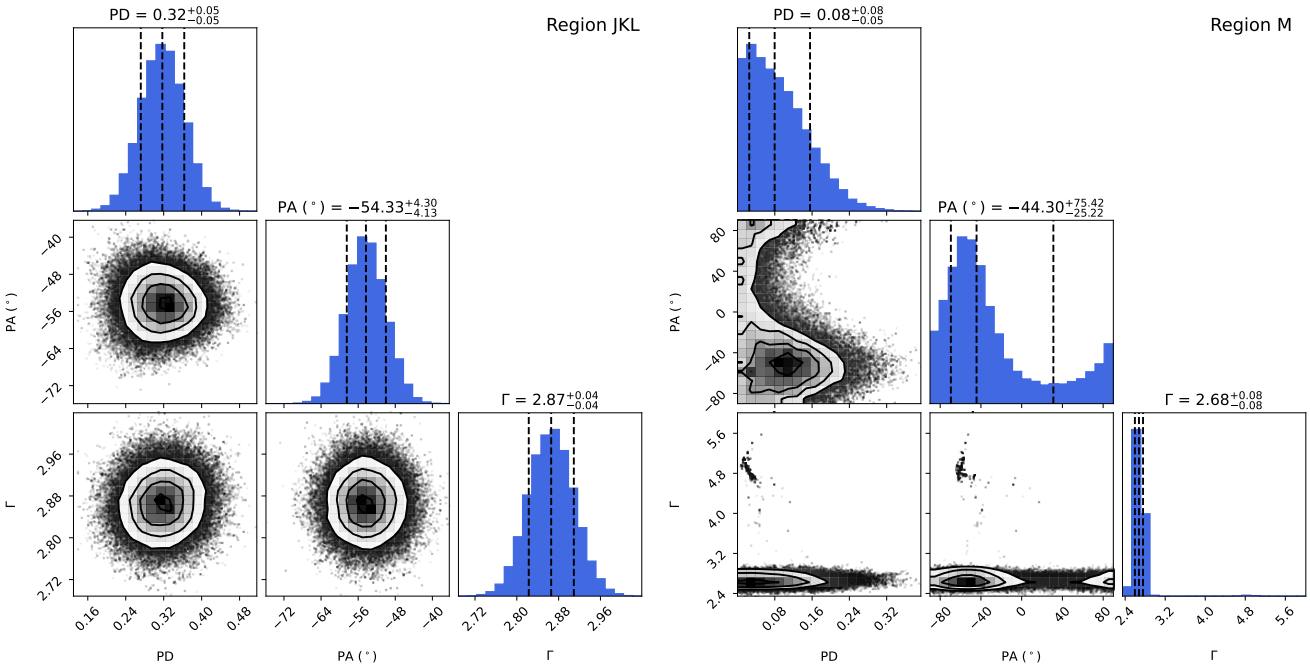

Figure 9. Two-dimensional correlation distributions of parameters in the spectropolarimetric analysis for regions JKL (left) and M (right). The contours provide the 0.5σ, 1σ, 1.5σ, and 2σ equivalent range. The histograms show the posterior distribution of PD, PA, and spectral index Γ, and the vertical lines denote the 0.16, 0.5, and 0.84 quantiles of the samples.

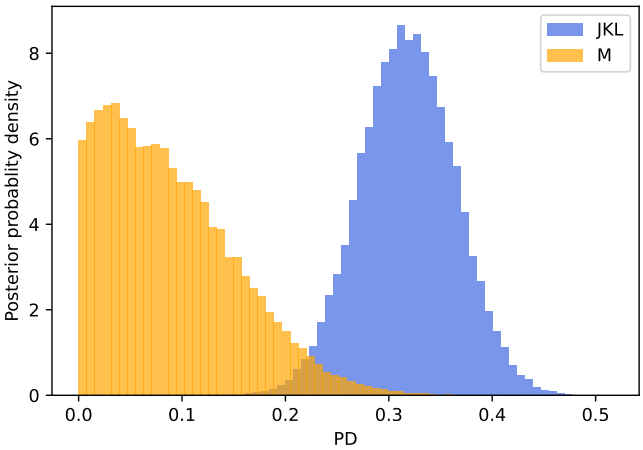

Figure 10. Posterior distribution of PD in regions "JKL" and "M".

ORCID iDs

Ping Zhou https://orcid.org/0000-0002-5683-822X
Patrick Slane https://orcid.org/0000-0002-6986-6756
Dmitry Prokhorov https://orcid.org/0000-0001-6511-4330
Jacco Vink https://orcid.org/0000-0002-4708-4219
Riccardo Ferrazzoli https://orcid.org/0000-0003-1074-8605
William Cotton https://orcid.org/0000-0001-7363-6489
Niccolò Bucciantini https://orcid.org/0000-0002-8848-1392
Yi-Jung Yang https://orcid.org/0000-0001-9108-573X
Stefano Silvestri https://orcid.org/0000-0002-8665-0105
Douglas A. Swartz https://orcid.org/0000-0002-2954-4461
Philip Kaaret https://orcid.org/0000-0002-3638-0637
Enrico Costa https://orcid.org/0000-0003-4925-8523
C.-Y. Ng https://orcid.org/0000-0002-5847-2612
Estela Reynoso https://orcid.org/0000-0002-1875-7701
Paolo Soffitta https://orcid.org/0000-0002-7781-4104
Allyn F. Tennant https://orcid.org/0000-0002-9443-6774
Wenlang He https://orcid.org/0009-0002-4427-6976

References

Acero, F., Ballet, J., & Decourchelle, A. 2007, A&A, 475, 883
Acero, F., Aharonian, F., Akhperjanian, A. G., et al. 2010, A&A, 516, A62
Arnaud, K. A. 1996, in ASP Conf. Ser. 101, Astronomical Data Analysis Software and Systems V, ed. G. H. Jacoby & J. Barnes (San Francisco, CA: ASP), 17
Asplund, M., Grevesse, N., Sauval, A. J., & Scott, P. 2009, ARA&A, 47, 481
Astropy Collaboration, Price-Whelan, A. M., Sipőcz, B. M., et al. 2018, AJ, 156, 123
Astropy Collaboration, Price-Whelan, A. M., Lim, P. L., et al. 2022, ApJ, 935, 167
Astropy Collaboration, Robitaille, T. P., Tollerud, E. J., et al. 2013, A&A, 558, A33
Baldini, L., Bucciantini, N., Lalla, N. D., et al. 2022, SoftX, 19, 101194
Bell, A. R. 2004, MNRAS, 353, 550
Blasi, P. 2013, A&ARv, 21, 70
Bykov, A. M., Osipov, S. M., Uvarov, Y. A., Ellison, D. C., & Slane, P. 2024, PhRvD, 110, 023041
Caprioli, D., & Spitkovsky, A. 2014, ApJ, 783, 91
Chevalier, R. A., & Oishi, J. 2003, ApJL, 593, L23
Cotton, W. D., Kothes, R., Camilo, F., et al. 2024, ApJS, 270, 21
Di Marco, A., Soffitta, P., Costa, E., et al. 2023, AJ, 165, 143
Draine, B. T. 2011, Physics of the Interstellar and Intergalactic Medium (Princeton, NJ: Princeton Univ. Press)
Dubner, G., & Giacani, E. 2015, A&ARv, 23, 3
Dubner, G. M., Giacani, E. B., Goss, W. M., Green, A. J., & Nyman, L. Å. 2002, A&A, 387, 1047
Ferrazzoli, R., Slane, P., Prokhorov, D., et al. 2023, ApJ, 945, 52
Ferrazzoli, R., Prokhorov, D., & Bucciantini, N. 2024, ApJL, 967, L38
Foreman-Mackey, D., Hogg, D. W., Lang, D., & Goodman, J. 2013, PASP, 125, 306
Giuffrida, R., Miceli, M., Caprioli, D., et al. 2022, NatCo, 13, 5098
Goodman, J., & Weare, J. 2010, CAMCS, 5, 65
Inoue, T., Shimoda, J., Ohira, Y., & Yamazaki, R. 2013, ApJL, 772, L20
Joye, W. A., & Mandel, E. 2003, in ASP Conf. Ser. 295, Astronomical Data Analysis Software and Systems XII, ed. H. E. Payne, R. I. Jedrzejewski, & R. N. Hook (San Francisco, CA: ASP), 489
Katsuda, S., Petre, R., Long, K. S., et al. 2009, ApJL, 692, L105

Koo, B.-C., Kim, D., Yoon, S.-C., & Raymond, J. C. 2023, ApJ, 945, 158
Li, J.-T., Decourchelle, A., Miceli, M., Vink, J., & Bocchino, F. 2016, MNRAS, 462, 158
Mackay, D. J. C. 2003, Information Theory, Inference and Learning Algorithms (Cambridge: Cambridge Univ. Press)
Miceli, M., Acero, F., Dubner, G., et al. 2014, ApJL, 782, L33
O'C Drury, L., Duffy, P., & Kirk, J. G. 1996, A&A, 309, 1002
Parizot, E., Marcowith, A., Ballet, J., & Gallant, Y. A. 2006, A&A, 453, 387
Prokhorov, D. A., Yang, Y.-J., Ferrazzoli, R., et al. 2024, A&A, 692, A59
Ressler, S. M., Katsuda, S., Reynolds, S. P., et al. 2014, ApJ, 790, 85
Reynolds, S. P. 1998, ApJ, 493, 375
Reynolds, S. P., & Gilmore, D. M. 1986, AJ, 92, 1138
Reynoso, E. M., Hughes, J. P., & Moffett, D. A. 2013, AJ, 145, 104
Slane, P., Ferrazzoli, R., Zhou, P., & Vink, J. 2024, Galax, 12, 59
Smithsonian Astrophysical Observatory, 2000 SAOImage DS9: A Utility for Displaying Astronomical Images in the X11 Window Environment, Astrophysics Source Code Library, ascl:0003.002
Tanaka, T., Okuno, T., Uchida, H., et al. 2021, ApJL, 906, L3
Uchiyama, Y., Aharonian, F. A., Tanaka, T., Takahashi, T., & Maeda, Y. 2007, Natur, 449, 576
Vink, J. 2020, Physics and Evolution of Supernova Remnants (Berlin: Springer)
Vink, J., Kaastra, J. S., & Bleeker, J. A. M. 1996, A&A, 307, L41
Vink, J., & Laming, J. M. 2003, ApJ, 584, 758
Vink, J., Prokhorov, D., Ferrazzoli, R., et al. 2022, ApJ, 938, 40
Weisskopf, M. C., Soffitta, P., Baldini, L., et al. 2022, JATIS, 8, 026002
Williams, B. J., Borkowski, K. J., Ghavamian, P., et al. 2013, ApJ, 770, 129
Winkler, P. F., Gupta, G., & Long, K. S. 2003, ApJ, 585, 324
Winkler, P. F., & Long, K. S. 1997, ApJ, 491, 829
Winkler, P. F., Williams, B. J., Reynolds, S. P., et al. 2014, ApJ, 781, 65
Xing, Y., Wang, Z., Zhang, X., & Chen, Y. 2016, ApJ, 823, 44
Xu, S., & Lazarian, A. 2017, ApJ, 850, 126
Zhou, P., Chen, Y., Zhang, Z.-Y., et al. 2016, ApJ, 826, 34
Zhou, P., Prokhorov, D., Ferrazzoli, R., et al. 2023, ApJ, 957, 55